

Research Article

Open Access



The prediction of seismic amplification effect in three-dimensional sedimentary basins and its application

Zhenning Ba^{1,2,3}, Shaocong Mu³, Jingxuan Zhao³, Yushan Zhang⁴, Sanhong Chen⁴

¹State Key Laboratory of Hydraulic Engineering Simulation and Safety, Tianjin University, Tianjin 300350, China.

²Key Laboratory of Earthquake Engineering Simulation and Seismic Resilience of China Earthquake Administration, Tianjin 300350, China.

³School of Civil Engineering, Tianjin University, Tianjin 300350, China.

⁴China Earthquake Disaster Prevention Center, Beijing 100029, China.

Correspondence to: Prof. Zhenning Ba, School of Civil Engineering, Tianjin University, No. 135 Yaguan Road, Haihe Education Park, Tianjin 300354, China. E-mail: bazhenning_001@163.com

How to cite this article: Ba Z, Mu S, Zhao J, Zhang Y, Chen S. The prediction of seismic amplification effect in three-dimensional sedimentary basins and its application. *Dis Prev Res* 2023;2:19. <https://dx.doi.org/10.20517/dpr.2023.22>

Received: 30 Jun 2023 **First Decision:** 7 Sep 2023 **Revised:** 21 Sep 2023 **Accepted:** 16 Oct 2023 **Published:** 19 Oct 2023

Academic Editor: Yongbo Peng **Copy Editor:** Fangling Lan **Production Editor:** Fangling Lan

Abstract

Numerous studies have shown that the basin amplification effect is influenced by characteristic parameters such as basin geometry and media impedance contrast, but quantitative analysis of the effect for three-dimensional (3D) basins is still rare. In this paper, the basin amplification effect is quantified through an aggravation factor (AGF), which is defined as the ratio between 3D and 1D acceleration response spectra along the basin surface. Considering the 3D geometry of the actual basin, we investigate the sensitivity of aggravation factors to inclination angles, shape ratios, and impedance contrasts by establishing 78 3D trapezoidal sedimentary basin models with different characteristic parameters. Furthermore, we perform a statistical analysis of the aggravation factors and propose their prediction formulas, which are applied to the Euroseistest basin and the Shidian basin. The above analysis reveals that: (1) The effects of inclination angle and shape ratio on the aggravation factor are concentrated in the edge part and central part of the basin, respectively, while the impedance contrast has less influence on the aggravation factor along the basin surface; (2) From the prediction results for the Euroseistest basin, the aggravation factor of the 3D model is higher than that of the 2D model with a maximum error of 22%, while the distribution pattern of the aggravation factor along the surface is similar; and (3) The predicted results for the Shidian basin show that the basin with a small inclination angle has a larger aggravation factor in the edge part and



© The Author(s) 2023. **Open Access** This article is licensed under a Creative Commons Attribution 4.0 International License (<https://creativecommons.org/licenses/by/4.0/>), which permits unrestricted use, sharing, adaptation, distribution and reproduction in any medium or format, for any purpose, even commercially, as long as you give appropriate credit to the original author(s) and the source, provide a link to the Creative Commons license, and indicate if changes were made.



even exceeds the central part; for example, the highest aggravation factor is 2.155 in the edge part of the basin with an inclination angle of 6°.

Keywords: Three-dimensional sedimentary basin, seismic motion, characteristic parameters, amplification effect, aggravation factors

INTRODUCTION

As a typical complex site, the significant amplification of ground motion in sedimentary basins has been confirmed in multiple seismic surveys and strong earthquake observations^[1-4]. Many large cities (e.g., Tokyo, Beijing, Los Angeles, Mexico City, *etc.*) are built on the basins. Once a destructive earthquake occurs, it would cause terrible loss of life and property. In recent years, in the background of frequent global earthquakes and the development of the “resilient city”, it is important to conduct research on the seismic effects of sedimentary basins and quantitatively evaluate the seismic ground motions, aiming to ensure engineering seismic safety and promote the construction of resilient cities.

Due to the special geometry of the basin and the impedance difference between the media inside and outside the basin, the seismic waves are entrapped by the basin to generate complex wavefields, leading to various basin effects: (1) basin-edge effect^[5-7]; (2) focusing effect^[8-10]; and (3) resonance effect^[11,12]. The determination of seismic fortification parameters in the Seismic Ground Motion Parameter Zonation Map of China (GB18306-2015)^[13] and Code for Seismic Design of Buildings (GB50011-2010)^[14] are based on 1D horizontally layered sites. However, the simplified 1D seismic response analysis cannot involve the propagation of surface waves and other basin effects in the basin. Furthermore, Eurocode 8^[15] in Europe and the International Existing Building Code^[16] in America make allowance implicitly for 1D sites but overlook complex 2D or three-dimensional (3D) site effects due to irregular subsurface geometry. Therefore, it is necessary to conduct 2D or 3D research on the basin effects. The main content of this necessity of conducting 2D or 3D research on the basin effects focuses on irregular subsurface geometry and surface topography. The irregular underground geometric shape mainly affects the propagation of seismic waves within the soil, including reflection and refraction at the interface of the medium, while the surface topography mainly affects the propagation and attenuation of seismic waves on the surface.

At present, research approaches for basin effects include observation, analytical, and numerical methods. Although an observation method^[17-19] can provide the most realistic seismic records, it relies on a dense and extensive station distribution and is costly to collect huge amounts of data. The advantage of the analytical method^[20,21] is to analyze and explain the site ground motion characteristics essentially, but it is difficult to give the corresponding analytical solutions in heterogeneous media with irregular subsurface configurations. In recent years, the rapid development of computing technology has facilitated the progress of numerical methods for modeling complex geological structures in two or three dimensions, including finite-difference methods (FDM)^[6,22,23], finite-element methods (FEM)^[24-26], boundary element methods (BEM)^[27-29], spectral element methods (SEM)^[30,31], *etc.*

Based on the above-mentioned numerical approaches, numerous studies have been conducted on the influence of basin characteristic parameters on basin effects. Semblat *et al.* analyzed the amplification of seismic motion in terms of level^[28], occurring frequency, and location in 2D alluvial basins at different depths using the BEM. Lee *et al.* used the SEM to simulate strong ground motion throughout the Taipei metropolitan area and concluded that the amplification of ground motion was mainly controlled by basin depth and shallow shear wave velocity^[31]. Vessia *et al.* investigated the effect of basin shape ratios and sediment impedance contrasts on the amplification effect of 2D trapezoidal valleys using the FEM^[24].

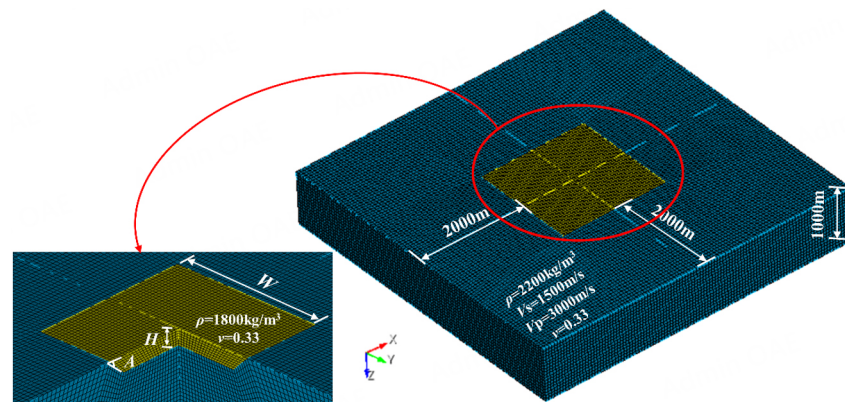


Figure 1. The model of a three-dimensional sedimentary basin.

Riga *et al.* studied the effect of different parameters related to basin geometry and dynamic soil properties on the additional amplification effect of the basin using the FDM^[22]. Moczo *et al.* performed 3D, 2D, and 1D simulations for six typical sedimentary valleys of various widths and depths and investigated the sensitivity of earthquake ground motion characteristics to impedance contrast^[23], attenuation, velocity gradient, and geometry. Qiang *et al.* investigated the effects of structural parameters on seismic aggravation of two-dimensional sedimentary valleys using the FEM^[26]. Due to the limitation of computational effort and calculation methods, 2D simplified models are mostly used to study the influence of basin characteristics parameters on the basin amplification effect in existing studies, while 3D models are often applied to simulate the actual basin under scenario earthquake, and few people have used 3D simplified models to analyze the basin amplification effect. Since the actual sedimentary basin is in 3D space, compared with the 2D model, the 3D model can consider a variety of basin effects more comprehensively and realistically and give a more accurate and reliable quantitative relationship between basin aggravation factors and characteristic parameters. Tong *et al.* pointed out in their study of seismic amplification in the Santa Monica region that considering the concentration of damage and the patterns of high amplification, the proper treatment of the problem must take 3D subsurface structures into account^[12]. For all these reasons, 3D basin models are established in this study.

In this paper, we investigate the sensitivity of aggravation factors to inclination angles, shape ratios, sediment thicknesses, and impedance contrasts by establishing 78 3D trapezoidal sedimentary basin models with different characteristic parameters. First of all, we qualitatively analyze the influence of basin characteristic parameters on the aggravation factor of the 3D basin. Then, the basins are divided into several regions, and the aggravation factors of each region are quantitatively analyzed to provide prediction formulas for aggravation factors. Finally, the prediction formulas are applied to the Euroseistest basin and the Shidian basin in order to provide a reference for local seismic motion estimation.

MODELING AND METHODOLOGY

To discuss the effects of different geometric and media parameters on the seismic response of the basins, we establish 3D trapezoidal sedimentary basin models located in a semi-infinite space, as shown in [Figure 1](#). A total of 78 basin models are formed by combining different basin widths W , sediment thicknesses H , inclination angles A , and sediments shear wave velocity V_s , while the media parameters of bedrock of all models are the same. Due to the fact that the sediment density, bedrock density, and bedrock wave velocity remain constant, different sediment wave velocities represent different impedance contrasts. The sediment-bedrock impedance contrast α defined as the ratio between the seismic impedance (that is, the

multiplication of density and shear wave velocity) of the sediments and the bedrock. The media parameters, including shear wave velocity V_s , compression wave velocity V_p , density ρ , and Poisson's ratio ν of the media inside and outside the basin, are listed in Table 1. Each model is encoded under a unique ID in the form $W_i H_j V_{sl} A_k$ [Table 2], indicating different combinations of widths, thicknesses, shear wave velocities, and inclination angles. The ID and characteristic parameters of all models are shown in Table 3, where the shape ratio Sr is defined as the ratio between the maximum thickness of the sedimentary layer and the half of basin width, $Sr = 2H/W$, and T_0 is the 1D fundamental period at the center of the basin, $T_0 = 4H/V_s$.

To simulate the effects of sedimentary basins on seismic wave propagation and scattering, the FK-SE method, which combines the frequency-wavenumber domain^[32] and the SEM^[33], is used to analyze the basin ground motion amplification effects. First, the semi-infinite space free-field response under the incident plane wave is calculated by the FK method, and then the equivalent nodal force input at the boundary of the spectral element is calculated; finally, the 3D complex wavefield is solved by the high-precision SEM. The wavefield at the combination of FK and SEM is determined according to the reference^[34]; i.e., the wavefield U_{total} at the boundary position is composed of two parts, the incident wavefield U_{FK} calculated by the FK method and the scattered wavefield U_{SC} in the region, when the scattered wave propagates outward from the calculation area and passes through the boundary, as shown in Equation (1). At the boundary of the SEM calculation region, the incident wavefield is subtracted from the total wavefield at the outer edge of the calculation domain, and only the absorption boundary condition is applied to the remaining scattered wavefield.

$$U_{total} = U_{FK} + U_{SC} \quad (1)$$

To ensure the accuracy of the SEM, it is required that the seismic wave contains at least five GLL nodes per wavelength. This means that the size of the elements d and the polynomial order N are both constrained by the shortest wavelength λ_{min} propagated in the media, and they should satisfy Equation (2)^[33].

$$d \leq \frac{N}{5} \cdot \lambda_{min} \quad (2)$$

The grid size of the sedimentary part is 30 m, and the maximum grid size outside the basin is 80 m. The total number of spectral elements in the model is 870,829, and the maximum frequency of simulation is 5 Hz.

A profile of the 3D model is cut along the xOz plane, and 101 receivers are evenly arranged from left to right along the basin surface. The 3D numerical simulations of the seismic response of all models, along with the corresponding 1D analyses of the isolated soil columns, are performed using as input acceleration the Gaussian pulse, as shown in Figure 2 in both frequency and time domains, as vertically incident plane SV waves. The bandwidth of the Gaussian pulse is 0~5 Hz. Then, the acceleration time history of the response of each receiver is obtained with the Gaussian pulse as input motion, which is further used to calculate the transfer functions of each receiver. In the end, the transfer functions are convolved with actual seismic waves to form a synthetic set of acceleration time histories.

INPUT GROUND MOTIONS

The selection of the input ground motion record should be based on several criteria: (1) motion recorded on rock or stiff soil sites; (2) magnitude range; (3) wide distribution of peak frequencies of the peak

Table 1. Properties of the simulation model

Category	ID code	ρ (kg/m ³)	V_s (m/s)	V_p (m/s)	Q_s	Q_p	ν
Basin	V_{s_1}	1,800	300	600	30	60	0.33
	V_{s_2}	1,800	400	800	40	80	0.33
	V_{s_3}	1,800	500	1,000	50	100	0.33
Rock	-	2,200	1,500	3,000	9,999	9,999	0.33

Q_s : The quality factors of S-wave, and $Q_s = V_s/10$; Q_p : the quality factors of P-wave, and $Q_p = V_p/10$; ν : Poisson's ratio, and $\nu = (\gamma^2 - 2)/2(\gamma^2 - 1)$, in which $\gamma = V_p/V_s$.

Table 2. Nomenclature of the ID code for each model

i, j, k, l	W_i (m)	H_j (m)	A_k (°)	V_{s_l} (m/s)
1	2,000	100	20	300
2	3,000	200	45	400
3	4,000	400	65	500

acceleration response spectrum within the considered frequency range; and (4) sufficient number of records for a meaningful statistical analysis. Based on the above standards, ten seismic acceleration records are selected from the Pacific Earthquake Engineering Research Center (PEER Available from: <https://ngawest2.berkeley.edu/>) as the input motion, which are recorded at rock or stiff soil sites with a wide distribution of peak frequencies of the peak acceleration response spectrum within the considered frequency range, involving different magnitudes, fault types, epicentral distances, and peak accelerations (PGA). The detailed parameters of the selected ten acceleration records are shown in Table 4. The selected acceleration records are low-pass filtered at 5 Hz, and the ten acceleration records and the normalized acceleration response spectra ($\zeta = 0.05$) after the filtering process are shown in Figure 3. The curve of the CSDB-II is the seismic design response spectra for Class II Sites of Code for Seismic Design of Buildings.

AGGRAVATION FACTOR

The aggravation factor is used to characterize the basin amplification effect, which is widely adopted in many studies^[23,27,35-39]. It is defined as the ratio between the acceleration response spectra of the 3D basin model and the corresponding 1D model surface observation points. The 78 3D basin models and the corresponding 1D models in Table 3 are numerically simulated; 101 observation points are evenly located on the basin surface, and ten actual acceleration records are input for each, as shown in Figure 3. A total of $78 \times 2 \times 101 \times 10 = 157,560$ ground acceleration time courses is synthesized by numerical simulations. Due to the symmetry of basin models, the seismic response of one-half of the receivers is analyzed in the following. The acceleration response spectra are obtained from the simulated acceleration time series, and the 3D results are compared with the 1D results to obtain the aggravation factor AGF_m as follows:

$$AGF_m(T/T_0, X/W) = \frac{SA_{3D,m}(T/T_0, X/W)}{SA_{1D,m}(T/T_0, X/W)} \quad (3)$$

$$AGF(T/T_0, X/W) = \frac{\sum_{m=1}^{10} AGF_m(T/T_0, X/W)}{10} \quad (4)$$

where m is the input motion number; T/T_0 is the ratio of the period T to the fundamental period T_0 of the 1D soil column in the middle of the basin; X/W is the ratio of the distance X from the basin surface receiver to the basin bedrock junction to the basin width W ; $SA_{3D,m}(T/T_0, X/W)$ and $SA_{1D,m}(T/T_0, X/W)$ represent the

Table 3. Geometrical and dynamic properties of all models

Model ID	W	H	A	Vs	Sr	T ₀	Model ID	Wm	H	A	Vs	Sr	T ₀
W ₁ H ₁ V _{s1} A ₁	2,000	100	20	300	0.10	1.33	W ₂ H ₂ V _{s3} A ₁	3,000	200	20	500	0.13	1.60
W ₁ H ₁ V _{s1} A ₂	2,000	100	45	300	0.10	1.33	W ₂ H ₂ V _{s3} A ₂	3,000	200	45	500	0.13	1.60
W ₁ H ₁ V _{s1} A ₃	2,000	100	65	300	0.10	1.33	W ₂ H ₂ V _{s3} A ₃	3,000	200	65	500	0.13	1.60
W ₁ H ₁ V _{s2} A ₁	2,000	100	20	400	0.10	1.00	W ₂ H ₃ V _{s1} A ₁	3,000	400	20	300	0.27	5.33
W ₁ H ₁ V _{s2} A ₂	2,000	100	45	400	0.10	1.00	W ₂ H ₃ V _{s1} A ₂	3,000	400	45	300	0.27	5.33
W ₁ H ₁ V _{s2} A ₃	2,000	100	65	400	0.10	1.00	W ₂ H ₃ V _{s1} A ₃	3,000	400	65	300	0.27	5.33
W ₁ H ₁ V _{s3} A ₁	2,000	100	20	500	0.10	0.80	W ₂ H ₃ V _{s2} A ₁	3,000	400	20	400	0.27	4.00
W ₁ H ₁ V _{s3} A ₂	2,000	100	45	500	0.10	0.80	W ₂ H ₃ V _{s2} A ₂	3,000	400	45	400	0.27	4.00
W ₁ H ₁ V _{s3} A ₃	2,000	100	65	500	0.10	0.80	W ₂ H ₃ V _{s2} A ₃	3,000	400	65	400	0.27	4.00
W ₁ H ₂ V _{s1} A ₁	2,000	200	20	300	0.20	2.67	W ₂ H ₃ V _{s3} A ₁	3,000	400	20	500	0.27	3.20
W ₁ H ₂ V _{s1} A ₂	2,000	200	45	300	0.20	2.67	W ₂ H ₃ V _{s3} A ₂	3,000	400	45	500	0.27	3.20
W ₁ H ₂ V _{s1} A ₃	2,000	200	65	300	0.20	2.67	W ₂ H ₃ V _{s3} A ₃	3,000	400	65	500	0.27	3.20
W ₁ H ₂ V _{s2} A ₁	2,000	200	20	400	0.20	2.00	W ₃ H ₁ V _{s1} A ₁	4,000	100	20	300	0.05	1.33
W ₁ H ₂ V _{s2} A ₂	2,000	200	45	400	0.20	2.00	W ₃ H ₁ V _{s1} A ₂	4,000	100	45	300	0.05	1.33
W ₁ H ₂ V _{s2} A ₃	2,000	200	65	400	0.20	2.00	W ₃ H ₁ V _{s1} A ₃	4,000	100	65	300	0.05	1.33
W ₁ H ₂ V _{s3} A ₁	2,000	200	20	500	0.20	1.60	W ₃ H ₁ V _{s2} A ₁	4,000	100	20	400	0.05	1.00
W ₁ H ₂ V _{s3} A ₂	2,000	200	45	500	0.20	1.60	W ₃ H ₁ V _{s2} A ₂	4,000	100	45	400	0.05	1.00
W ₁ H ₂ V _{s3} A ₃	2,000	200	65	500	0.20	1.60	W ₃ H ₁ V _{s2} A ₃	4,000	100	65	400	0.05	1.00
W ₁ H ₃ V _{s1} A ₂	2,000	400	45	300	0.40	5.33	W ₃ H ₁ V _{s3} A ₁	4,000	100	20	500	0.05	0.80
W ₁ H ₃ V _{s1} A ₃	2,000	400	65	300	0.40	5.33	W ₃ H ₁ V _{s3} A ₂	4,000	100	45	500	0.05	0.80
W ₁ H ₃ V _{s2} A ₂	2,000	400	45	400	0.40	4.00	W ₃ H ₁ V _{s3} A ₃	4,000	100	65	500	0.05	0.80
W ₁ H ₃ V _{s2} A ₃	2,000	400	65	400	0.40	4.00	W ₃ H ₂ V _{s1} A ₁	4,000	200	20	300	0.10	2.67
W ₁ H ₃ V _{s3} A ₂	2,000	400	45	500	0.40	3.20	W ₃ H ₂ V _{s1} A ₂	4,000	200	45	300	0.10	2.67
W ₁ H ₃ V _{s3} A ₃	2,000	400	65	500	0.40	3.20	W ₃ H ₂ V _{s1} A ₃	4,000	200	65	300	0.10	2.67
W ₂ H ₁ V _{s1} A ₁	3,000	100	20	300	0.07	1.33	W ₃ H ₂ V _{s2} A ₁	4,000	200	20	400	0.10	2.00
W ₂ H ₁ V _{s1} A ₂	3,000	100	45	300	0.07	1.33	W ₃ H ₂ V _{s2} A ₂	4,000	200	45	400	0.10	2.00
W ₂ H ₁ V _{s1} A ₃	3,000	100	65	300	0.07	1.33	W ₃ H ₂ V _{s2} A ₃	4,000	200	65	400	0.10	2.00
W ₂ H ₁ V _{s2} A ₁	3,000	100	20	400	0.07	1.00	W ₃ H ₂ V _{s3} A ₁	4,000	200	20	500	0.10	1.60
W ₂ H ₁ V _{s2} A ₂	3,000	100	45	400	0.07	1.00	W ₃ H ₂ V _{s3} A ₂	4,000	200	45	500	0.10	1.60
W ₂ H ₁ V _{s2} A ₃	3,000	100	65	400	0.07	1.00	W ₃ H ₂ V _{s3} A ₃	4,000	200	65	500	0.10	1.60
W ₂ H ₁ V _{s3} A ₁	3,000	100	20	500	0.07	0.80	W ₃ H ₃ V _{s1} A ₁	4,000	400	20	300	0.20	5.33
W ₂ H ₁ V _{s3} A ₂	3,000	100	45	500	0.07	0.80	W ₃ H ₃ V _{s1} A ₂	4,000	400	45	300	0.20	5.33

$W_2H_1Vs_3A_3$	3,000	100	65	500	0.07	0.80	$W_3H_3Vs_1A_3$	4,000	400	65	300	0.20	5.33
$W_2H_2Vs_1A_1$	3,000	200	20	300	0.13	2.67	$W_3H_3Vs_2A_1$	4,000	400	20	400	0.20	4.00
$W_2H_2Vs_1A_2$	3,000	200	45	300	0.13	2.67	$W_3H_3Vs_2A_2$	4,000	400	45	400	0.20	4.00
$W_2H_2Vs_1A_3$	3,000	200	65	300	0.13	2.67	$W_3H_3Vs_2A_3$	4,000	400	65	400	0.20	4.00
$W_2H_2Vs_2A_1$	3,000	200	20	400	0.13	2.00	$W_3H_3Vs_3A_1$	4,000	400	20	500	0.20	3.20
$W_2H_2Vs_2A_2$	3,000	200	45	400	0.13	2.00	$W_3H_3Vs_3A_2$	4,000	400	45	500	0.20	3.20
$W_2H_2Vs_2A_3$	3,000	200	65	400	0.13	2.00	$W_3H_3Vs_3A_3$	4,000	400	65	500	0.20	3.20

5% damped acceleration response spectra for 3D and 1D results at each input motion, respectively. Therefore, $AGF_m(T/T_0, X/W)$ represents the aggravation factor dependent on the dimensionless period T/T_0 and the location parameter X/W at each input motion. To reduce the influence of the uncertainty of the input ground motions with different characteristics on the aggravation factors, the arithmetic mean of the basin aggravation factor $AGF(T/T_0, X/W)$ is calculated according to Equation (4) over the ten aggravation factors.

Qualitative analysis of aggravation factor

Figure 4 shows the effect of inclination angles, thicknesses, widths, and impedance contrasts on the $AGF(T/T_0, X/W)$ for selected models in order to help understand the way each one of the examined parameters affects AGF . The aggravation factors present a significantly variant behavior in its spatial distribution accompanied by a change in inclination angle, as shown in Figure 4A. Comparing the results of $W_1H_2Vs_2A_2$ and $W_1H_2Vs_2A_3$ models, we can see that the effect of inclination angle on the AGF is mainly concentrated in the edge part, and the effect on the central part is not obvious. It is noteworthy that a large amplification phenomenon still occurs in the central part of $W_1H_2Vs_2A_1$. The possible reason is that the inclination angle and width of this model are small, and the surface waves excited in the wide edge part propagate a short distance to the central part, resulting in obvious amplification phenomena with a maximum aggravation factor of 2.84. In addition, the AGF is less than 1.0 in some areas of the edge part, showing the characteristic of reduction; i.e., the 3D response is smaller than the corresponding 1D response, and the larger the inclination angle, the smaller the AGF , and the more obvious the characteristic of reduction. The reason may be that in the 1D analysis, due to the difference in media impedance contrast, the incident body wave is reflected back and forth within the sedimentary media several times, resulting in a larger site response, while in the 3D models, the incident wave is refracted at the slope of the basin edge and part of the energy is transmitted to the interior of the basin, and the larger inclination angle, the more energy is transmitted to the interior of the basin after refraction, and the site response is, thus, reduced.

It can be seen that the period and location distribution of the aggravation factor AGF for different basin widths is in Figure 4B. In wide basins, the maximum value of AGF occurs close to the change in sediment thickness at the basin edge ($X/W = 0.2$), and in narrow basins, the maximum value of AGF is closer to the middle region of the basin ($X/W = 0.4$). The AGF in the narrow basin model reaches a maximum value of 2.34, which is significantly higher than the results for the larger width basins. The reason is that the surface waves excited by the edge of the basin propagate toward the center of the basin and continuously decay with the propagation distance. In models with larger widths, the aggravation factor in the central part is close to 1.0. In addition, as the width increases, the

Table 4. Description of input seismic records

ID	Record number	Earthquake	Station	Magnitude	Fault type	R_{rup} (km)	PGA (cm/s^2)	V_{30} (m/s)
In1	59	San Fernando	Cedar Springs_ Allen Ranch	6.61	Reverse	89.72	17.5	813.48
In2	765	Loma Prieta	Gilroy Array #1	6.93	Reverse oblique	9.64	154.5	1,428.14
In3	1,050	Northridge-01	Pacoima Dam (downstr)	6.69	Reverse	4.92	187.2	2,016.13
In4	1,108	Kobe_Japan	Kobe University	6.9	Strike-slip	0.9	275.8	1,043
In5	1,161	Kocaeli_Turkey	Gebze	7.51	Strike-slip	7.57	257.6	792
In6	1,943	Anza-02	Idyllwild-Keenwild Fire Sta.	4.92	Normal oblique	32.12	16.8	845.41
In7	3,325	ChiChi_Taiwan-06	HWA003	6.3	Reverse	56.02	38.0	1,525.85
In8	4,097	Parkfield-02_CA	Slack Canyon	6.0	Strike-slip	2.99	206.7	648.09
In9	4,483	L'Aquila_Italy	L'Aquila - Parking	6.3	Normal	5.38	304.2	717
In10	8,165	Duzce_Turkey	IRIGM 496	7.14	Strike-slip	4.21	738.5	760

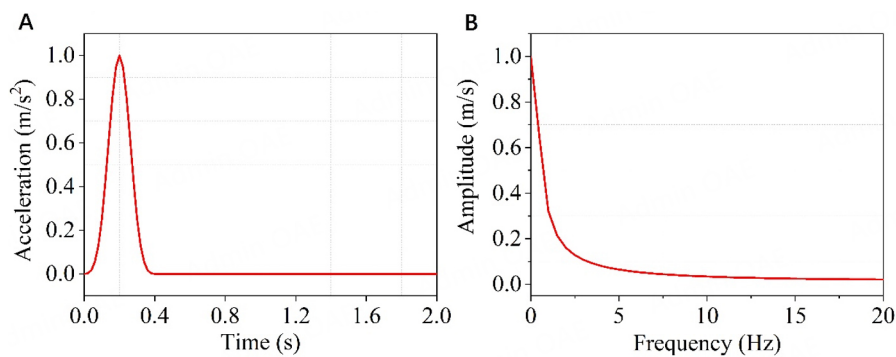


Figure 2. The acceleration time histories of the input pulse and Fourier amplitude spectrum of the pulse.

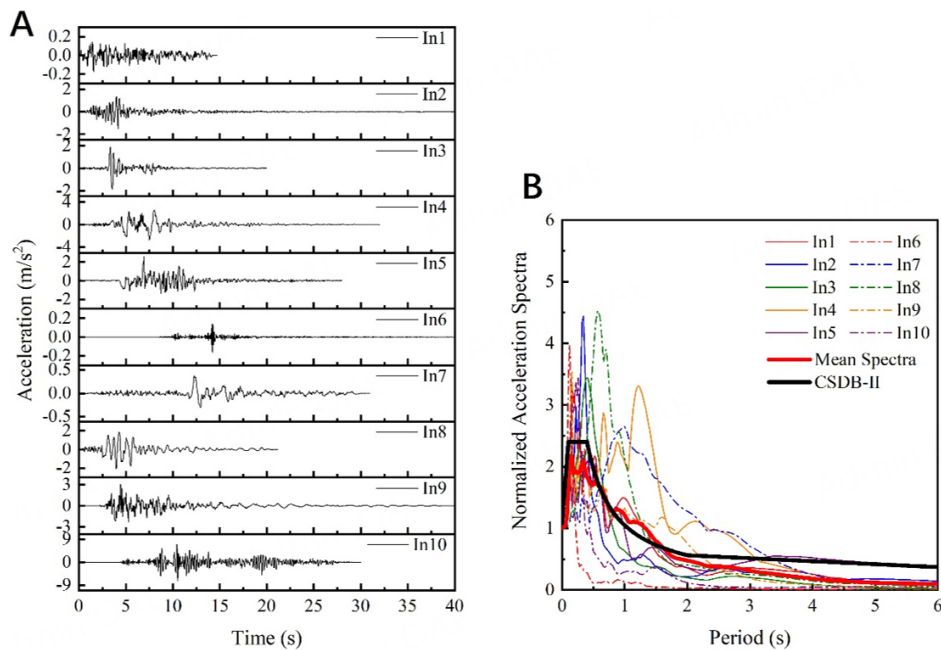


Figure 3. (A) Acceleration time histories of input seismic records and (B) corresponding normalized response spectra with respect to CSDB-II design spectra. CSDB-II: Class-II site of Code for Seismic Design of Buildings.

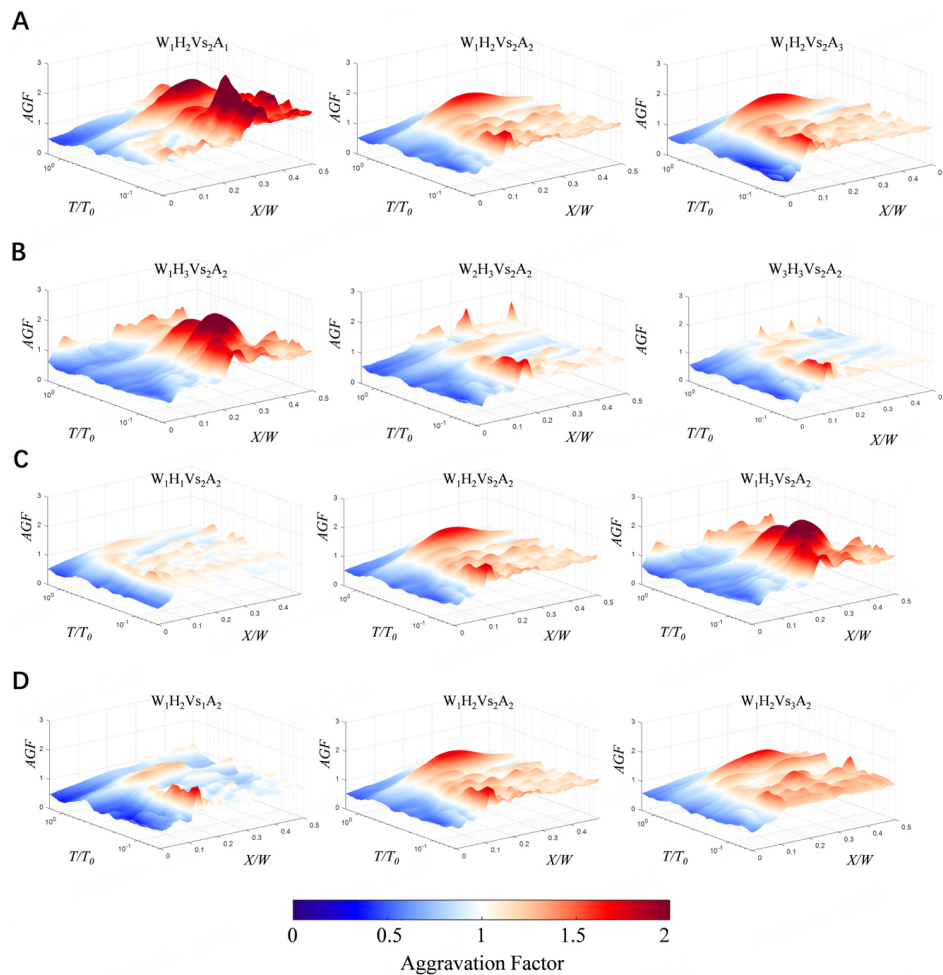


Figure 4. Aggravation factor $AGF(X/W, T/T_0)$ affected by (A) inclination angles, (B) widths, (C) thicknesses, (D) impedance contrasts along the half-width of the basin surface for selected symmetrical models.

proportion of the significant amplification area decreases, and its location gradually concentrates at the edge part of the basin.

Figure 4C indicates that there is a significant increase in AGF in the central region of the basin with increasing sediment thicknesses. Moreover, the reduction range in the basin edge part also expands with increasing sediment thickness; e.g., the reduction range ($AGF < 1$) is less than $0.1 W$ in $W_1H_1Vs_2A_2$ and $W_1H_2Vs_2A_2$, while the reduction range expands to $0.2 W$ in $W_1H_3Vs_2A_2$. The larger the sediment thickness at the same inclination angle, the larger the surface projection of the basin edge part, and the reduction phenomenon occurs in the projection range. In general, basin widths and sediment thicknesses (both can be attributed to shape ratio) mainly affect the response of the central part, and the amplification effect is stronger in the central part of the basin with a high shape ratio. It cannot be ignored that the thickness of the sediment also influences the response of the basin edge part.

The period and location distribution of the aggravation factor AGF for different impedance contrasts can be seen in **Figure 4D**. For the low impedance contrast basins, such as $W_1H_2Vs_1A_2$, the amplification is obvious only where the sediment thickness changes, while in higher impedance contrast basins, amplification is present in all central parts of the basin. The reason for this phenomenon is that seismic waves are slow to

attenuate in soils with high wave velocities, and the surface waves excited at the basin edge spread to the middle of the high wave velocity basin, causing ground motions to amplify. Meanwhile, as the impedance contrast increases, the level of reduction gradually decreases. Because the high impedance contrast media has a weaker ability to capture the wave, the incident wave is reflected by the ground surface and transmits out at the media interface, resulting in a reduced 1D response.

Quantitative analysis of aggravation factor

The above-mentioned studies and the actual seismic damage indicate that there are significant differences in the amplification effects of ground motions in different regions in the basin. Therefore, dividing the basin into several regions and statistically analyzing the aggravation factors within each region can avoid overestimating or underestimating the amplification effect of certain regions of the basin to a certain extent. The half-width of the symmetrical basin surface is divided into five regions (*a*, *b*, *c*, *d*, and *e*) with two equal-width regions (*a* and *b*) over the edge part of the basin and three equal-width regions (*c*, *d*, and *e*) over the central part of the basin [Figure 5]. The best-fit curves expressing the correlation of max *AGF* with the characteristics parameters for each region are estimated through regression analyses using the least squares method. Additionally, considering the poor fit of the data for certain parameters, a mean value of max *AGF* of each partition is further examined for each region. Additionally, the standard deviation (SD) is calculated, and the mean value ± 1 times the SD is used to measure the dispersion of the data.

The fitted relationship between inclination angles and max *AGF* is shown in Figure 6. In the basin edge part, max *AGF* decreases with increasing inclination angle and can be as low as 0.7 at $A = 65^\circ$, indicating that ground motion is significantly suppressed. The boxplot [Figure 6C] shows that the data dispersion at $A = 65^\circ$ is small, meaning that the conclusion is probably reliable. The coefficients of determination R^2 , which are used to characterize the degree of interpretation of the best-fit curves to the data, of the best-fit curves in regions *a* and *b* are 0.525 and 0.615, respectively. The max *AGF* exhibits a significant negative correlation with the inclination angle in regions *a* and *b*. While in the central part of the basin (Regions *c*, *d*, and *e*), the correlation between max *AGF* and the inclination angle is weakened, as the corresponding best-fit curves tend to be flat. However, it should be pointed out that our results differ from the findings of Riga^[22], whose study revealed that the aggravation factor of Region *a* is not significantly affected by inclination angles. The difference may be explained by the fact that the other characteristic parameters of the selected basin models are different, further reflecting the fact that the basin amplification effect is influenced by various factors.

The effect of shape ratios on max *AGF* is illustrated in Figure 7, and max *AGF* shows a tendency to increase with the increase of shape ratio throughout the basin surface. It should be noted that when fitting the max *AGF* curves in Regions *a* and *b*, the case of $Sr = 0.4$ is not involved because there is a lack of data with $A = 20^\circ$ in the case of $Sr = 0.4$. As discussed in the previous section, the inclination angle has a significant impact on max *AGF* in regions *a* and *b*. To avoid missing data interfering with the results, the case of $Sr = 0.4$ is not considered. By comparing the coefficients of determination of the best-fit curve related to inclination angle and shape ratio, it is found that max *AGF* is more affected by the inclination angle in the edge part of the basin, while max *AGF* is more affected by shape ratio in the central part.

The effect of impedance contrast on max *AGF* is illustrated in Figure 8. The best-fit curves of max *AGF* in all regions of the basin are relatively flat. The 95% confidence bands for max *AGF* lie between 0.9 and 1.2 in the edge part (regions *a*, *b*), while the 95% confidence bands for max *AGF* lie between 1.2 and 1.7 in the central part (regions *c*, *d*, *e*). The amplification effect in the central part is usually higher than that in the edge part, which is also shown in the previous discussions on inclination angle and shape ratio. As can be

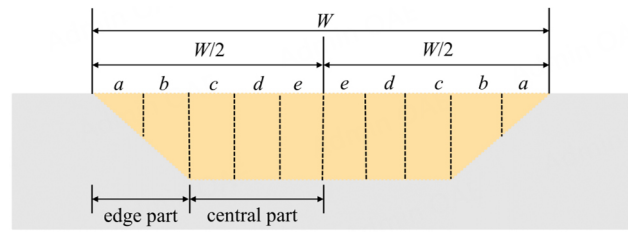


Figure 5. Division of symmetrical basins into five regions.

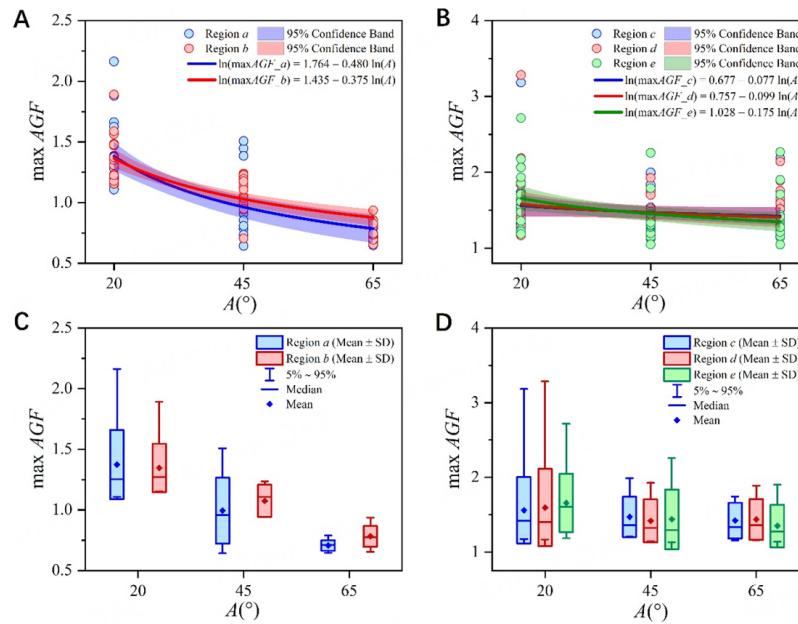


Figure 6. Influence of inclination angle on max AGF for five regions: (A) best-fit curves for regions *a, b*; (B) best-fit curves for regions *c, d, e*; (C) boxplot of max AGF for regions *a, b*; (D) boxplot of max AGF for regions *c, d, e*.

seen from the boxplots, the max AGF shows a poor correlation with the impedance contrast because the same impedance contrast is used in the 3D model and the corresponding 1D model.

Difference in aggravation factors between 2D and 3D

The fitting results based on 3D simulations are compared with the 2D results of Riga^[22], as shown in Figure 9. Except for Region *a*, 3D results are larger than 2D results in other regions. Given that the basins with higher shape ratios are modeled ($Sr = 0.2 \sim 0.4$) in our research and that higher shape ratio basins tend to have larger max AGF, it is bound to have an impact on the comparison. Therefore, when comparing the differences in the influence of inclination angle on max AGF between 2D and 3D, more attention should be paid to the changing trend. In the central part of the basin (regions *c, d, e*), the 3D results show a certain decreasing trend, but the 2D results suggest that max AGF basically does not vary with inclination angles. Probably, Riga adopted larger basin widths, resulting in the surface waves excited at the basin slope not reaching the central part of the basin. The curves of the effect of shape ratios on max AGF demonstrate that max AGF increases with the increase of shape ratios for both 2D and 3D results. In Region *a*, 2D results are higher than 3D results at low shape ratios, and 3D results are higher than 2D results at high shape ratios. Yet, the situation in Region *e* is the opposite of Region *a*.

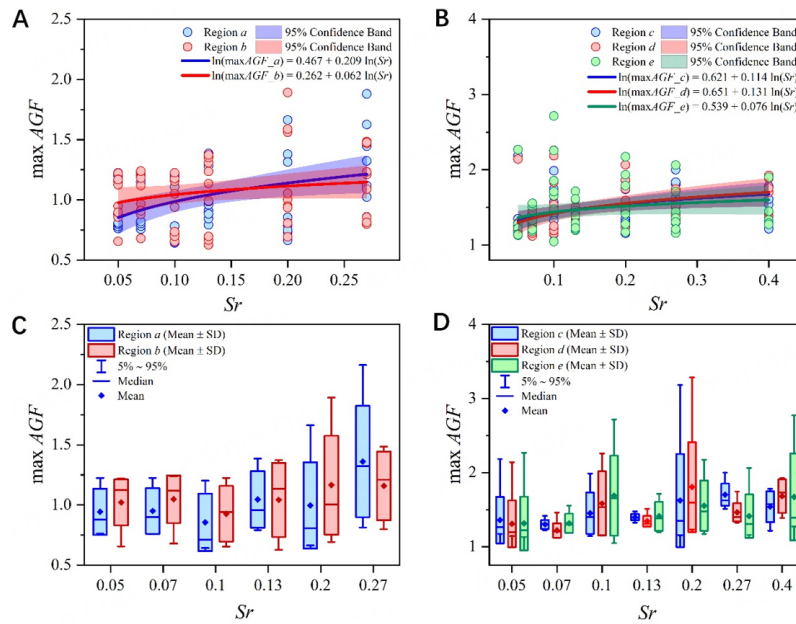


Figure 7. Influence of shape ratio on $\max AGF$ for five regions: (A) best-fit curves for regions a, b ; (B) best-fit curves for regions c, d, e ; (C) boxplot of $\max AGF$ for regions a, b ; (D) boxplot of $\max AGF$ for regions c, d, e .

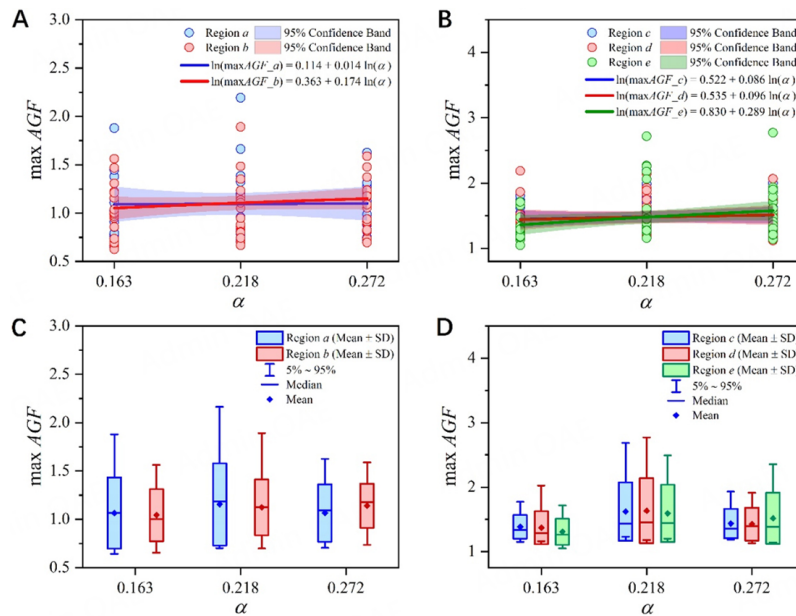


Figure 8. Influence of impedance contrast on $\max AGF$ for five regions: (A) best-fit curves for regions a, b ; (B) best-fit curves for regions c, d, e ; (C) boxplot of $\max AGF$ for regions a, b ; (D) boxplot of $\max AGF$ for regions c, d, e .

APPLICATION OF AGGRAVATION FACTOR PREDICTION FORMULA

The best-fit formulas for basin aggravation factors in different regions with respect to each parameter (inclination angles, shape ratios, and impedance contrasts) are listed in Table 5. The influence weight w of each parameter on $\max AGF$ is calculated based on the coefficient of determination R^2 of each best-fit curve, and the prediction equation for $\max AGF$ in each region containing three parameters is obtained according to Equation (5):

$$\begin{cases} w(A) = \frac{R^2(A)}{R^2(A) + R^2(Sr) + R^2(\alpha)} \\ w(Sr) = \frac{R^2(Sr)}{R^2(A) + R^2(Sr) + R^2(\alpha)} \\ w(\alpha) = \frac{R^2(\alpha)}{R^2(A) + R^2(Sr) + R^2(\alpha)} \\ \max AGF(A, Sr, \alpha) = w(A) \max AGF(A) + w(Sr) \max AGF(Sr) + w(\alpha) \max AGF(\alpha) \end{cases} \quad (5)$$

where $w(A)$, $w(Sr)$, and $w(\alpha)$ are the influence weight of inclination angles, shape ratios, and impedance contrasts, respectively. Based on the above prediction equations, after determining the inclination angle, shape ratio, and impedance contrast, the predicted values of the corresponding aggravation factors can be calculated to predict the amplification effect of the basin.

Prediction of aggravation factors in the Euroseistest basin

The Euroseistest basin is an approximately symmetrical cross-section of the Mygdonian basin, a sedimentary basin located in Thessaloniki, Northern Greece, which was established in 1993 as a test site for seismological and earthquake engineering research. Zhu *et al.* developed a simplified 2D model of the Euroseistest basin and simulated the distribution of aggravation factors within the surface area of the basin^[40], as shown in Figure 10. According to the simplified model, it is known that inclination angle $A = 8^\circ$, shape ratio $Sr = 0.08$, impedance contrast $\alpha = 0.177$, and the comparative analysis of the predicted values of the aggravation factor and the results of Zhu are shown in Figure 10. It can be seen that the distribution pattern of the aggravation factor along the surface is basically consistent. However, except for Region *a*, the prediction values of the remaining four regions are overestimated, probably because the surface receivers of the 3D model are additionally influenced by waves coming from outside the plane where the profile is located. Other possible reasons need an in-depth discussion, such as attempting to eliminate interference from waves in other directions in the 3D model.

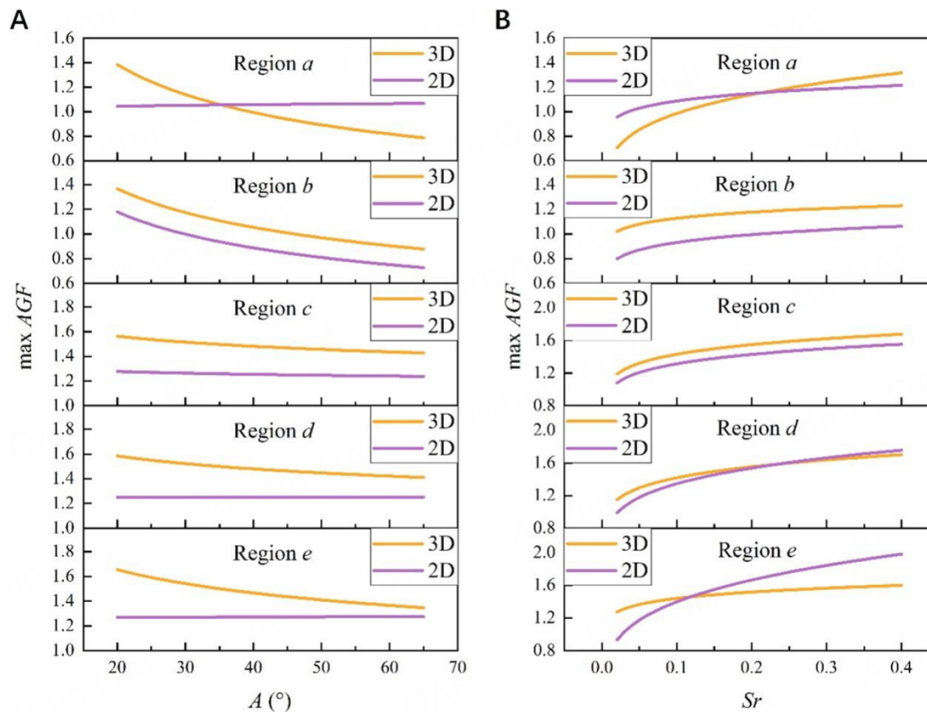
Prediction of aggravation factors in the Shidian basin

The Shidian basin is located in the western region of Yunnan Province, China, and has occurred high intensity anomalies numerous times during historically strong earthquakes. The 1976 Longling earthquake, the 1988 Lancang-Gengma earthquake, and the 2001 Shidian earthquake have caused serious damage in this basin, although the epicenters of these earthquakes are located tens to hundreds of kilometers from the basin^[41]. Based on the soil samples and wave velocity measuring results from 24 boreholes in the basin, Liu *et al.* provided some typical stratigraphic sections and the 3D velocity structure model of the Shidian basin^[42]. According to the 3D velocity structure model, three typical profiles are selected in order from north to south. The first profile is located in the transition area from shallow to deep sediment thickness in the basin, and the second and third profiles are located deeper inside the basin. The second profile is more symmetrical on both sides, and the third profile is asymmetrical. The position and bedrock shape of each profile are shown in Figure 11. The irregular bedrock shapes are simplified to trapezoids, and the inclination angle and shape ratio of the simplified model are recorded. On the other hand, the multi-layer soil with different wave velocities in the basin is simplified to single-layer soil, and the simplified shear wave velocity is calculated according to Equation (6).

$$\bar{V}_s = \frac{\sum_{i=1}^n V_{s_i} H_i}{\sum_{i=1}^n H_i} \quad (6)$$

Table 5. Fitting formulas for the maximum aggravation factor in each region

Parameters	Regions ID	Best-fit formulas	R^2	w
Inclination angle	<i>a</i>	$\ln(\max AGF) = 1.764 - 0.480 \ln(A)$	0.525	0.791
	<i>b</i>	$\ln(\max AGF) = 1.435 - 0.375 \ln(A)$	0.615	0.902
	<i>c</i>	$\ln(\max AGF) = 0.677 - 0.077 \ln(A)$	0.030	0.186
	<i>d</i>	$\ln(\max AGF) = 0.757 - 0.099 \ln(A)$	0.038	0.224
	<i>e</i>	$\ln(\max AGF) = 1.028 - 0.175 \ln(A)$	0.114	0.538
Shape ratio	<i>a</i>	$\ln(\max AGF) = 0.467 + 0.209 \ln(Sr)$	0.138	0.208
	<i>b</i>	$\ln(\max AGF) = 0.262 + 0.062 \ln(Sr)$	0.043	0.063
	<i>c</i>	$\ln(\max AGF) = 0.621 + 0.114 \ln(Sr)$	0.124	0.770
	<i>d</i>	$\ln(\max AGF) = 0.651 + 0.131 \ln(Sr)$	0.125	0.735
	<i>e</i>	$\ln(\max AGF) = 0.539 + 0.076 \ln(Sr)$	0.040	0.189
Impedance contrast	<i>a</i>	$\ln(\max AGF) = 0.114 + 0.014 \ln(\alpha)$	0.001	0.001
	<i>b</i>	$\ln(\max AGF) = 0.363 + 0.174 \ln(\alpha)$	0.024	0.035
	<i>c</i>	$\ln(\max AGF) = 0.522 + 0.086 \ln(\alpha)$	0.007	0.044
	<i>d</i>	$\ln(\max AGF) = 0.535 + 0.096 \ln(\alpha)$	0.007	0.041
	<i>e</i>	$\ln(\max AGF) = 0.830 + 0.289 \ln(\alpha)$	0.058	0.273

**Figure 9.** Comparison of best-fit curves of max AGF between (A) 3D result derived from this study and (B) 2D result derived from Riga et al.^[22].

The simplified basin characteristics parameters are shown in Table 6, which are applied to the aggravation factor prediction equation to predict the amplification effect of the Shidian basin. It should be noted that for the asymmetric basin, both half-widths need to be partitioned into regions, with the region numbers $a_1 \sim e_1$ and $a_2 \sim e_2$, respectively, and the partitioning rules are the same as those for the symmetric basin. The predicted values of max AGF for different regions of each profile are shown in Table 7 and Figure 12. The bold represents the maximum aggravation factor in each region of the corresponding profile model in

Table 6. Simplified profile characteristics parameters

Profiles number	Inclination angle (°)		Shape ratio	Impedance contrast
	Left	Right		
Profile 1	11	6	0.09	0.176
Profile 2	12	12	0.10	0.185
Profile 3	35	15	0.11	0.188

Table 7. Predicted values of max AGF for different regions of each profile

Regions ID	max AGF		
	Profile 1	Profile 2	Profile 3
a_1	1.662	1.607	1.048
a_2	2.155		1.468
b_1	1.647	1.599	1.106
b_2	2.041		1.479
c_1	1.457	1.468	1.457
c_2	1.472		1.475
d_1	1.464	1.475	1.451
d_2	1.487		1.480
e_1	1.637	1.630	1.467
e_2	1.748		1.597

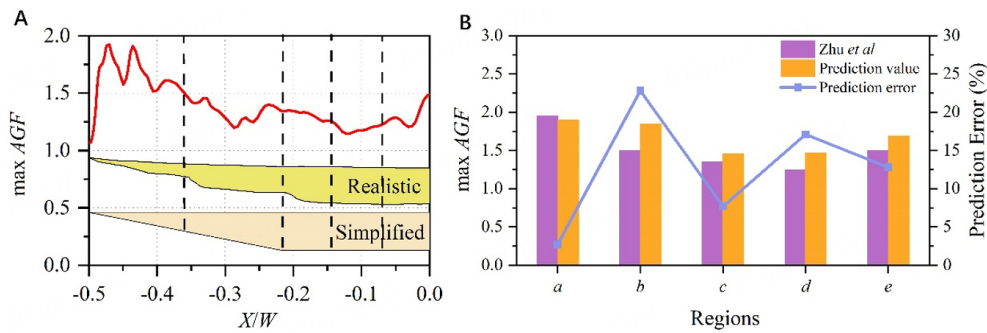


Figure 10. (A) Aggravation factor of the simplified Euroseistest 2D model derived from Zhu et al.^[40]; (B) Comparison between 3D predicted results and 2D results derived from Zhu et al.^[40].

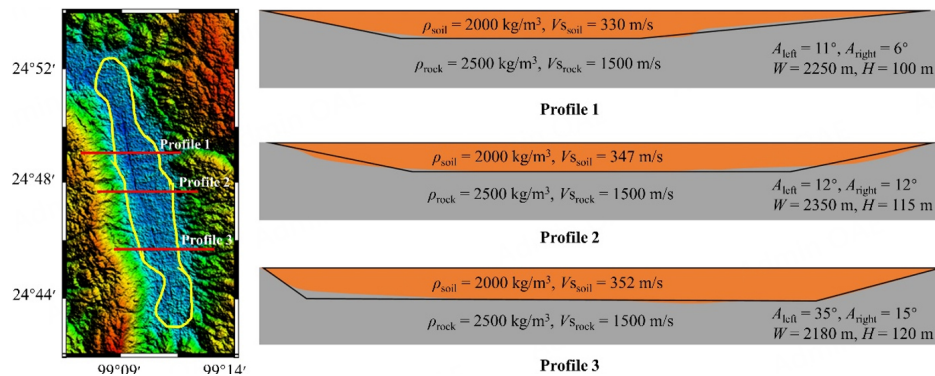


Figure 11. Shidian basin and three selected profiles.

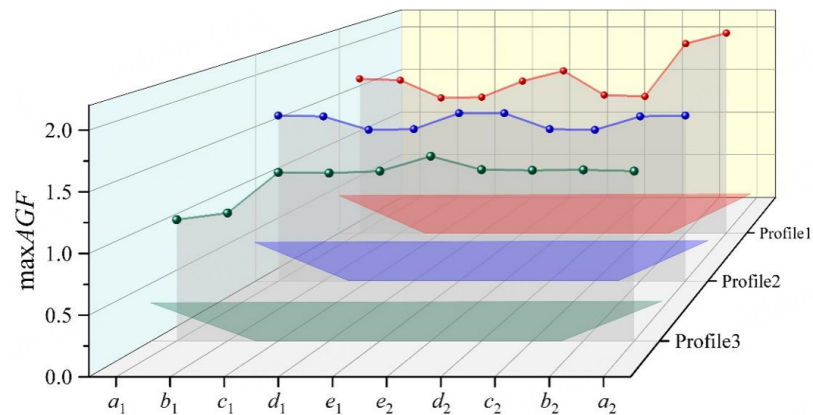


Figure 12. Predicted values of max *AGF* for different regions of each profile.

Table 7. For profile 1, the maximum value of max *AGF* (around 2.155) occurs in Region a_2 ; for profiles 2 and 3, the maximum value of max *AGF* occurs in Region e_2 with 1.630 and 1.597, respectively. The difference between the max *AGF* of the edge part and the central part is not significant in profile 2, while the max *AGF* of the central part is significantly higher than that of the edge part in profile 3. It can be concluded that the basin with a small inclination angle has a larger aggravation factor in the edge part and even exceeds the central part. When the inclination angle increases to a certain degree, the aggravation factor in the central region is higher than that in the edge region.

CONCLUSION

Currently, research on the impact of basin characteristic parameters on basin effects generally adopts simplified two-dimensional models or 3D models of specific basins, and few people have used 3D simplified models to analyze the basin amplification effect. Compared with the 2D model, the 3D model can more comprehensively investigate basin effects. Therefore, we established 78 3D sedimentary basin models to study the amplification effect of basins with different geometric and physical parameters. Basin-induced amplification is quantified through a period-dependent and location-dependent aggravation factor (*AGF*), defined as the ratio between 3D and 1D acceleration response spectra at some points on the basin surface. The basins are divided into several regions, and the aggravation factors of each region are quantitatively analyzed to provide prediction formulas for aggravation factors, which are applied to the Euroseistest basin and the Shidian basin. The main conclusions are as follows:

- (1) The effect of inclination angles on the *AGF* is mainly concentrated in the edge part, and max *AGF* increases with decreasing inclination angles.
- (2) The seismic motion in the edge part of the basin with a small inclination angle is significantly amplified. The reason is that when the inclination angle is small, the incident wave excites a more complex wave field over a wider range of the edge slope, and the refraction of the body wave caught in the sediments is more complicated between the media partition interface and the ground surface.
- (3) The seismic motion in the edge part of the basin with a large inclination angle is obviously suppressed. The reason may be that some of the incident waves are refracted at a large angle in a steep basin slope and then propagate toward the interior of the basin, leading to the reduction of the surface response in the edge part.

(4) Basin width and sediment thickness (both can be attributed to shape ratios) mainly affect the response of the central part, and the amplification effect is stronger in the central part of the basin with a high shape ratio.

(5) The poor fitting of the aggravation factor curve regarding the impedance contrast indicates that the amplification effect does not correlate well with the impedance contrast. The aggravation factor, as the ratio between the 3D response and the 1D response, is not significantly affected by the impedance contrast because the same impedance contrast is used in the 3D model and the corresponding 1D model.

(6) From the prediction results for the Euroseistest basin, the distribution pattern of the aggravation factor along the surface is basically similar. Nevertheless, the aggravation factor of the 3D model is higher than that of the 2D model because the surface observation points are additionally influenced by waves coming from outside the plane of the 2D model.

(7) The predicted results for the Shidian basin show that the basin with a small inclination angle has a larger aggravation factor in the edge part and even exceeds the central part; when the inclination angle increases to a certain degree, the aggravation factor in the central region is higher than that in the edge region.

The prediction formula we proposed involves four parameters, including inclination angles, widths, sediment thicknesses, and impedance contrasts, which can be easily obtained through geological structure exploration, making it convenient to serve as a reference indicator for evaluating basin effects in practical engineering. However, it is necessary to point out some limitations of this study. On the one hand, the nonlinearity of the soil was not considered in this study. As mentioned above, more than 100,000 ground motions were obtained by using the convolution method based on the linear constitutive model of the soil. If the nonlinearity is considered, it would require large computational efforts to obtain such a large amount of ground motion data. In addition, the nonlinearity will affect both 1D and 3D results, so the effect on the aggravation factor may not be significant. However, there is no doubt that considering the nonlinearity of soil in studying seismic motion in future research is more reasonable, especially in soft soil sites. On the other hand, in order to appropriately reduce the number of computational models, only three different scenarios were considered for inclination angles, depths, widths, and impedance contrasts. It should be acknowledged that setting more scenarios can make the prediction formula more accurate, but the conclusions of this study are correct. Finally, this study only considers ideal trapezoidal sedimentary basins under incident plane waves. However, the actual bedrock shape, topography, and incident wave field are usually more complex. In the future, further research will be conducted on more complex conditions.

DECLARATIONS

Authors' contributions

Conceptualization, methodology, validation, formal analysis, resources, supervision, project administration: Ba Z

Software, investigation, data curation: Mu S, Zhao J

Methodology, writing - original draft, visualization: Mu S, Zhang Y, Chen S

Availability of data and materials

Not applicable.

Financial support and sponsorship

Financial support from the National Natural Science Foundation of China (Grant #52178495) is gratefully acknowledged.

Conflicts of interest

All authors declared that there are no conflicts of interest.

Ethical approval and consent to participate

Not applicable.

Consent for publication

Not applicable.

Copyright

© The Author(s) 2023.

REFERENCES

1. Anderson JG, Bodin P, Brune JN, et al. Strong ground motion from the michoacan, Mexico, earthquake. *Science* 1986;233:1043-9. [DOI](#)
2. Chen K. Strong ground motion and damage in the Taipei basin from the moho reflected seismic waves during the March 31, 2002, Hualien, Taiwan earthquake. *Geophys Res Lett* 2003;30:1151-4. [DOI](#)
3. Pitarka A, Irikura K, Iwata T, Sekiguchi H. Three-dimensional simulation of the near-fault ground motion for the 1995 Hyogo-Ken Nanbu (Kobe), Japan, earthquake. *Bull Seismol Soc Am* 1998;88:428-40. [DOI](#)
4. Wald DJ, Graves RW. The seismic response of the Los Angeles basin, California. *Bull Seismol Soc Am* 1998;88:337-56. [DOI](#)
5. Kawase H. The cause of the damage belt in Kobe: "the basin-edge effect," constructive interference of the direct S-wave with the basin-induced diffracted/rayleigh waves. *Seismol Res Lett* 1996;67:25-34. [DOI](#)
6. Graves RW, Pitarka A, Somerville PG. Ground-motion amplification in the Santa Monica area: effects of shallow basin-edge structure. *Bull Seismol Soc Am* 1998;88:1224-42. [DOI](#)
7. Stewart JP, Chiou S, Bray JD, Graves RW, Somerville PG, Abrahamson NA. Ground motion evaluation procedures for performance-based design. *Soil Dynam Earthq Eng* 2002;22:765-72. [DOI](#)
8. Gao S, Liu H, Davis PM, Knopoff L. Localized amplification of seismic waves and correlation with damage due to the Northridge earthquake: evidence for focusing in Santa Monica. *Bull Seismol Soc Am* 1996;86:S209-30. [DOI](#)
9. Alex CM, Olsen KB. Lens-effect in Santa Monica? *Geophys Res Lett* 1998;25:3441-4. [DOI](#)
10. Davis PM, Rubinstein JL, Liu KH, Gao SS, Knopoff L. Northridge earthquake damage caused by geologic focusing of seismic waves. *Science* 2000;289:1746-50. [DOI](#) [PubMed](#)
11. Bard P, Bouchon M. The two-dimensional resonance of sediment-filled valleys. *Bull Seismol Soc Am* 1985;75:519-41. [DOI](#)
12. Tong J, Kuribayashi E. The three-dimensional resonance of axisymmetric sediment-filled valleys. *Soils Found* 1988;28:130-46. [DOI](#)
13. General administration of quality supervision, inspection and quarantine of the People's Republic of China. Seismic ground motion parameters zonation map of China (GB18306-2015). Beijing: China Standard Press; 2015.
14. Ministry of housing and urban-rural development of the People's Republic of China, general administration of quality supervision, inspection and quarantine of the People's Republic of China. Code for seismic design of buildings (GB50011-2010). Beijing: China Architecture & Building Press; 2010.
15. Eurocode 8: design of structures for earthquake resistance - part 1: general rules, seismic actions and rules for buildings. European Standard EN 1998-1: 2004.
16. International Code Council. 2012 international existing building code; 2011. Available from: <https://codes.iccsafe.org/content/IEBC2012/effective-use-of-the-international-existing-building-code> [Last accessed on 19 Oct 2023]
17. Frankel A, Hough S, Friberg P, Busby R. Observations of Loma Prieta aftershocks from a dense array in Sunnyvale, California. *Bull Seismol Soc Am* 1991;81:1900-22. [DOI](#)
18. Bindi D, Parolai S, Cara F, et al. Site amplifications observed in the gubbio basin, central Italy: hints for lateral propagation effects. *Bull Seismol Soc Am* 2009;99:741-60. [DOI](#)
19. Bindi D, Luzi L, Parolai S, Di Giacomo D, Monachesi G. Site effects observed in alluvial basins: the case of Norcia (Central Italy). *Bull Earthq Eng* 2011;9:1941-59. [DOI](#)
20. Trifunac MD. Surface motion of a semi-cylindrical alluvial valley for incident plane SH waves. *Bull Seismol Soc Am* 1971;61:1755-70. [DOI](#)
21. Todorovska MI, Lee VW. A note on response of shallow circular valleys to Rayleigh waves: analytical approach. *Earthq Eng Eng Vib*

- 1990;10:21-34. Available from: https://www.researchgate.net/publication/244968419_A_Note_on_Response_of_Shallow_Circular_Valleys_to_Rayleigh_Waves_Analytical_Approach [Last accessed on 19 Oct 2023]
22. Riga E, Makra K, Pitilakis K. Aggravation factors for seismic response of sedimentary basins: a code-oriented parametric study. *Soil Dynam Earthq Eng* 2016;91:116-32. DOI
 23. Moczo P, Kristek J, Bard P, et al. Key structural parameters affecting earthquake ground motion in 2D and 3D sedimentary structures. *Bull Earthq Eng* 2018;16:2421-50. DOI
 24. Vessia G, Russo S. Relevant features of the valley seismic response: the case study of Tuscan Northern Apennine sector. *Bull Earthq Eng* 2013;11:1633-60. DOI
 25. Riga E, Makra K, Pitilakis K. Investigation of the effects of sediments inhomogeneity and nonlinearity on aggravation factors for sedimentary basins. *Soil Dynam Earthq Eng* 2018;110:284-99. DOI
 26. Qiang S, Wang H, Wen R, Liu Q, Zhou Y. Investigating the effects of structural parameters on seismic aggravation of two-dimensional sedimentary valleys. *Soil Dynam Earthq Eng* 2023;171:107964. DOI
 27. Kawase H, Aki K. A study on the response of a soft basin for incident S, P, and Rayleigh waves with special reference to the long duration observed in Mexico City. *Bull Seismol Soc Am* 1989;79:1361-82. Available from: <https://pubs.geoscienceworld.org/ssa/bssa/article-abstract/79/5/1361/119226/A-study-on-the-response-of-a-soft-basin-for> [Last accessed on 19 Oct 2023].
 28. Semblat J, Dangla P, Kham M, Duval A. Seismic site effects for shallow and deep alluvial basins: in-depth motion and focusing effect. *Soil Dynam Earthq Eng* 2002;22:849-54. DOI
 29. Semblat J, Duval A, Dangla P. Seismic site effects in a deep alluvial basin: numerical analysis by the boundary element method. *Comput Geotech* 2002;29:573-85. DOI
 30. Komatitsch D. Simulations of ground motion in the Los Angeles basin based upon the spectral-element method. *Bull Seismol Soc Am* 2004;94:187-206. DOI
 31. Lee S, Chen H, Liu Q, Komatitsch D, Huang B, Tromp J. Three-dimensional simulations of seismic-wave propagation in the Taipei basin with realistic topography based upon the spectral-element method. *Bull Seismol Soc Am* 2008;98:253-64. DOI
 32. Cao Z, Tao X, Tao Z, Tang A. Kinematic source modeling for the synthesis of broadband ground motion using the f-k approach. *Bull Seismol Soc Am* 2019;109:1738-57. DOI
 33. Cupillard P, Delavaud E, Burgos G, et al. RegSEM: a versatile code based on the spectral element method to compute seismic wave propagation at the regional scale. *Geophys J Int* 2012;188:1203-20. DOI
 34. Ba Z, Wu M, Liang J, Zhao J, Lee VW. A two-step approach combining FK with SE for simulating ground motion due to point dislocation sources. *Soil Dynam Earthq Eng* 2022;157:107224. DOI
 35. Chávez-garcía FJ, Faccioli E. Complex site effects and building codes: making the leap. *J Seismol* 2000;4:23-40. DOI
 36. Makra K, Chávez-garcía FJ, Raptakis D, Pitilakis K. Parametric analysis of the seismic response of a 2D sedimentary valley: implications for code implementations of complex site effects. *Soil Dynam Earthq Eng* 2005;25:303-15. DOI
 37. Kumar S, Narayan JP. Importance of quantification of local site effects based on wave propagation in seismic microzonation. *J Earth Syst Sci* 2008;117:731-48. DOI
 38. Makra K, Gelagoti F, Ktenidou OJ, Pitilakis K. Basin effects in seismic design: efficiency of numerical tools in reproducing complex seismic wavefields. Proceedings of the 12th World Conference on Earthquake Engineering; 2012 Sep 24-28; Lisbon, Portuga. 2012.
 39. Hasal ME, Iyisan R. A numerical study on comparison of 1D and 2D seismic responses of a basin in Turkey. *Am J Civ Eng* 2014;2:123. DOI
 40. Zhu C, Thambiratnam D, Gallage C. Statistical analysis of the additional amplification in deep basins relative to the 1D approach. *Soil Dynam Earthq Eng* 2018;104:296-306. DOI
 41. Liu Q, Yu Y, Zhang X. Three-dimensional simulations of strong ground motion in the Shidian basin based upon the spectral-element method. *Earthq Eng Eng Vib* 2015;14:385-98. DOI
 42. Liu Q, Li X, Sun P. Study on the 3-D velocity model of Shidian basin. *Earthq Eng Eng Dynam* 2013;33:88-94. (In Chinese). Available from: <https://pubs.cstam.org.cn/article/doi/10.11810/1000-1301.20130312> [Last accessed on 19 Oct 2023]